

Silver Nanocube Aggregates in Cylindrical Pores for Higher Refractive Index Plasmonic Sensing

Tobias König, Rajesh Kodiyath, Zachary A. Combs, Mahmoud. A. Mahmoud, Mostafa A. El-Sayed, and Vladimir V. Tsukruk*

We report on silver nanocubes (AgNCs) infiltrated into cylindrical nanopores of porous alumina membranes (PAM) with an outstanding chemical sensitivity based on refractive index sensing (RIS) measurements. Numerical simulations performed using the finite-difference time-domain (FDTD) method suggested that the enhanced sensitivity is based mainly on the inter-pore coupling plasmonic effect. This effect is related to plasmonic amplification based on localized surface plasmon resonance (LSPR) coupling between AgNCs located at the pore walls of neighboring cylindrical pores and separated by a nanoscale wall. Results are discussed for different aggregation scenarios ranging from individual nanocubes through pentamers on a flat glass surface, a flat alumina surface, and a concave local shape representing the experimental conditions. An experimental RIS sensitivity of about 770 nm per refractive index unit was found to be more than an order of magnitude higher for silver nanocube aggregates within cylindrical pores than that observed for ordinary planar substrates.

1. Introduction

It is well known that noble metallic nanoparticles excite strong resonant fields in the visible and infrared ranges when exposed to light due to the effect of localized surface plasmon resonances (LSPR).^[1] Recent interest in this field has surged with progress in the development of nanoparticle fabrication methods, their assembly into more complex nanostructures, as well as in the theoretical understanding of localized and coupling phenomena.^[2] The strong localized electric fields and coupling at nanojunctions have been used to facilitate colorimetric sensing and to dramatically increase the sensitivity via surface-enhanced Raman scattering (SERS)^[3] and fluorescence enhancement^[4] as well as to improve near-field imaging^[5] and energy conversion.^[6] The peak position of the LSPR bands

for noble metal nanoparticles is strongly dependent on nanoparticle size,^[7] shape,^[8] composition,^[9] and the refractive index of the surrounding media, or nanoparticles in their vicinity.

An increase in nanoparticle size facilitates surface charge separation, which results in an LSPR peak displacement to lower energy and higher local intensity fields.^[10] Moreover, significant improvements in sensitivity and applicability can be further achieved by tuning nanoparticle aggregation behavior and the precise geometry and dimensions of nanojunctions.^[11] The advantage of this approach is the strong resonant coupling of the nanoparticles within different aggregates.^[12] Nanoparticle arrays can produce tightly localized field enhancements facilitated by plasmon field coupling, which can be modulated by nanoparticle spacing.^[13]

However, the assembly of nanoparticles is difficult to control^[14] as well as the interpretation of the measured signal to the specific type of particle aggregation.^[15]

Most plasmonic-based sensing applications, such as SERS-active substrates or dark field microscopy, require the controlled aggregation of nanoparticles on a solid substrate.^[16] Generally, the condition where a nanoparticle is in direct contact with a solid substrate is a disadvantage for demanding sensing applications. For instance, a nanoparticle cannot be exposed to the external analyte on its substrate side, which leads to significant attenuation of LSPR phenomena.^[17] However, the presence of a solid substrate does break the symmetry of the primitive LSPR modes and results in the appearance of hybridized modes. This consequence of such an arrangement is particularly interesting for chemical sensing due to the possibility of different orientations of hybridized field modes, which can be generally separated into those orientated towards the substrate (dipole modes) and those orientated towards the medium (quadrupolar modes).^[18] Consequently, the quadrupolar mode might show higher sensitivity capability.^[19]

The use of anisotropic or non-spherically shaped nanostructures can further improve sensing ability. The charge separation and plasmonic intensity could be further increased for nanostructures with high aspect ratios^[20] or nanostructures with sharp edges such as nanostars or nanorods.^[21] A further step that can be taken to increase sensitivity is to use hollowed nanostructures, such as gold nanoshells^[22] or nanorice.^[9] The choice

Dr. T. König, Dr. R. Kodiyath, Z. A. Combs,
Prof. V. V. Tsukruk
School of Materials Science and Engineering
Georgia Institute of Technology
Atlanta, GA 30332-0245, USA
E-mail: vladimir@mse.gatech.edu

Dr. M. A. Mahmoud, Prof. M. A. El-Sayed
Laser Dynamics Laboratory, School of Chemistry and Biochemistry,
Georgia Institute of Technology
Atlanta, GA 30332-0400, USA



DOI: 10.1002/ppsc.201300217

of nanoparticle material and shape is also crucial for the control and monitoring of LSPR mode positions, intensities, and environmentally induced shifts.^[13] Nanocubes and nanoframes with sharp edges are considered to be promising candidates for sensing applications due to their high LSPR intensities and the presence of multiple modes under specific conditions.^[23] A higher sensitivity can be reached by using perfect cubes with no edge rounding and a small cube-to-cube distance.^[24] To date, however, only very limited attempts of using these nanostructures beyond traditional dispersions and on flat solid substrates have been reported.

In this article, we show that aggregation of silver nanocubes on different solid substrates can lead to substantial improvement of the refractive index sensitivity (RIS), which defines the chemical sensing ability. The experimentally observed plasmon mode excitations for an individual nanocube and for complex multiple cube aggregates are discussed with the assistance of finite-difference time-domain (FDTD) simulations. The results are compared with RIS measurements from a flat glass surface, a flat alumina surface, and a concave alumina substrate in relation to sensitive porous SERS substrates.^[3] Numerical simulations performed here suggest that the dramatically enhanced sensitivity observed experimentally for nanocubes in cylindrical alumina pores can largely be attributed to inter-pore coupling (IPC) of adjacent nanocube aggregates closely located across the ultrathin pore walls. An extraordinary experimental RIS sensitivity of about 770 nm per refractive index unit was found for such aggregates inside cylindrical pores, which is more than an order of magnitude higher than that observed earlier and calculated for nanocubes on planar solid substrates.

2. Materials and Methods

2.1. Experimental Section

2.1.1. Silver Nanocube Synthesis

AgNCs with 40 nm edge length were synthesized using the polyol method as described elsewhere.^[25] Briefly, in a 100 mL round bottom glass flask, 70 mL of ethylene glycol (EG) was heated to 150 °C for 1 h. Then, a solution of 0.85 g polyvinylpyrrolidone (PVP) dissolved in 10 mL EG was added to the hot EG. 0.4 mL of sodium sulfide (Na₂S) (3×10^{-3} M) dissolved in EG and 6 mL of 282×10^{-3} M silver nitrate dissolved in EG were injected into the reaction mixture. The reaction mixture was stirred at 200 rpm and refluxed at 150 °C for 10 min until the solution became opaque. In order to purify the AgNCs, 5 mL of the prepared AgNC solution was diluted with water and centrifuged at 10 000 rpm for 5 min. The precipitated AgNCs were then re-dispersed in water. The synthesized AgNCs were 40 ± 3 nm in size as statistically evaluated using transmission electron microscopy (TEM) images (see Supporting Information).

2.1.2. Assembly of AgNCs on Planar Substrates

AgNCs were assembled on glass and alumina substrates by drop casting. For the alumina substrates, a 1 μm thick layer

of alumina was coated onto glass slides using a Kurt J. Lesker Axxis electron beam deposition system. Approximately, 50 μL of the AgNC solution was drop cast on the substrates and allowed to dry in air.

2.1.3. PAM–AgNC Substrate

The immobilization of nanocubes on porous alumina membranes (PAMs) (Anodisc 47, Whatman) was done using a modified procedure from the literature.^[26,27] We utilized a positively charged polyelectrolyte, polyethylenimine (PEI, MW = 70000, Polysciences), for surface modification of the inner pore walls. A 0.2% aqueous solution of PEI was deposited on the pore walls by spin-coating at 3000 rpm for ≈40 s followed by rinsing with Nanopure water ($18.2 \text{ M}\Omega \text{ cm}^{-1}$). This procedure resulted in a 2–3 nm thick uniform polymer coating that was verified by atomic force microscopy (AFM) measurements. The AgNCs were loaded on the pore walls properly modified with proper layer-by-layer (LbL) coatings as suggested earlier.^[3,28,29] PAMs were decorated with AgNCs by vacuum infiltrating an aqueous suspension of AgNCs through a surface-modified PAM with a diameter of 47 mm, a cylindrical pore diameter of 243 ± 20 nm, average wall thickness of 40 nm (variation between 0 nm (contact) to about 100 nm), and a total depth of 60 μm. Substrates were sonicated and washed after vacuum infiltration to remove excess polymer and AgNCs adsorbed on the modified PAM surface. The concave alumina substrates were fabricated by mechanical breaking of the PAM. Thus, the cross-section (concave substrate) is an inside view of the PAM decoration with AgNCs.

2.1.4. UV–Vis Extinction Measurements

The UV–Vis extinction spectra of the flat glass and alumina substrates as well as the PAM–AgNC substrates were recorded on a Shimadzu UV-2450 spectrophotometer over a wavelength range of 300–800 nm in transmission mode. The substrates were positioned in a quartz UV–Vis cuvette so that the AgNC-functionalized area of the sample was exposed to the incident light. The UV–Vis absorption spectra of the concave alumina substrates (PAM cross-section) were collected using a CRAIC QDI 202 microspectrophotometer attached to a Leica DM 4000M microscope. The transmission mode of the Shimadzu UV–Vis spectrophotometer provides a higher resolution compared with the reflection mode of the CRAIC microscope. Additionally, we compared the UV–Vis results from the PAM substrate with the local CRAIC measurements (Figure S1, Supporting Information). However, the concave alumina substrate could be measured only in reflection mode with the CRAIC set-up due to the orientation specific experimental requirements.

In order to measure the RIS, the substrates were submerged in solvents of different refractive indices during UV measurements. In each case, a baseline measurement was done under the same experimental conditions with a non-functionalized substrate. We estimated the RIS values by changing the medium from air to water assuming the linear variation with refractive index, a common approach. The RIS is defined as the LSPR peak shift scaled by the refractive index change and the

figure of merit (FoM) is defined as the RIS scaled by the full width at half maximum (FWHM).^[30]

2.1.5. FDTD Simulations

Simulations of the extinction spectra, surface charge distributions, and the field intensity distributions, were done using commercial software from Lumerical Solutions Inc. (FDTD Solutions, Version 7.5.7 and 8.0.2). The edge rounding factor is defined as the edge radius scaled by the length of the nanocube. The experimentally measured edge rounding factor from TEM was $16 \pm 3\%$, which corresponds closely with the 15% edge rounding factor calculated from the dipole absorbance peak in solution. The edge rounding factor was statistically determined by circular approximation of TEM images of AgNCs (Figure S2, Supporting Information). The AgNCs were also covered by a PVP layer (index of 1.42) as described in the synthesis procedure, and the coating thickness was statistically determined to be 1.5 ± 0.3 nm.^[31] This thickness was estimated as 2 nm in FDTD simulations due to the integer mesh size limitations. Consequently, the minimum cube-to-cube distance was always 4 nm. The polymer coating was rounded at the cube edges to the same degree as the silver nanocube for simulations.

For silver permittivity, we used material data from Hagemann et al. (CRC approximation).^[32] We found a much better agreement with our experimentally measured extinction spectra by using the permittivity from CRC approximation instead of the more commonly used source from Johnson and Christy.^[33] The higher imaginary part in the permittivity from CRC approximation could be attributed to geometrical effects as Shalaev et al. have reported.^[34] A low imaginary part results in a more narrow LSPR peak with a high extinction cross-section. The silver permittivity was fitted with six coefficients and an RMS error of 0.23. The water permittivity data were taken from Palik^[35] and had an RMS error of 0.008. A simulation mesh size of 1 nm was chosen and the second conformal variant mesh refinement was used. For the best simulation stability, the mesh area was chosen to be 120 nm larger than the existing structure in all three principal directions. All simulations reached the auto shut off level of 10^{-5} before reaching 75 fs simulation time. For spectral peak fitting, we used the multiple Lorentzian peak fit function implemented in OriginPro 8.50 SR1. Spectral peak fitting of the simulated cross-section shows an R^2 value of 0.98 and the corresponding peak positions are summarized in Table S1 in the Supporting Information. To identify each cube mode, we used a surface charge plot.

3. Results and Discussion

In this study, we used optical extinction measurements in air and water to establish the refractive index sensitivity of silver

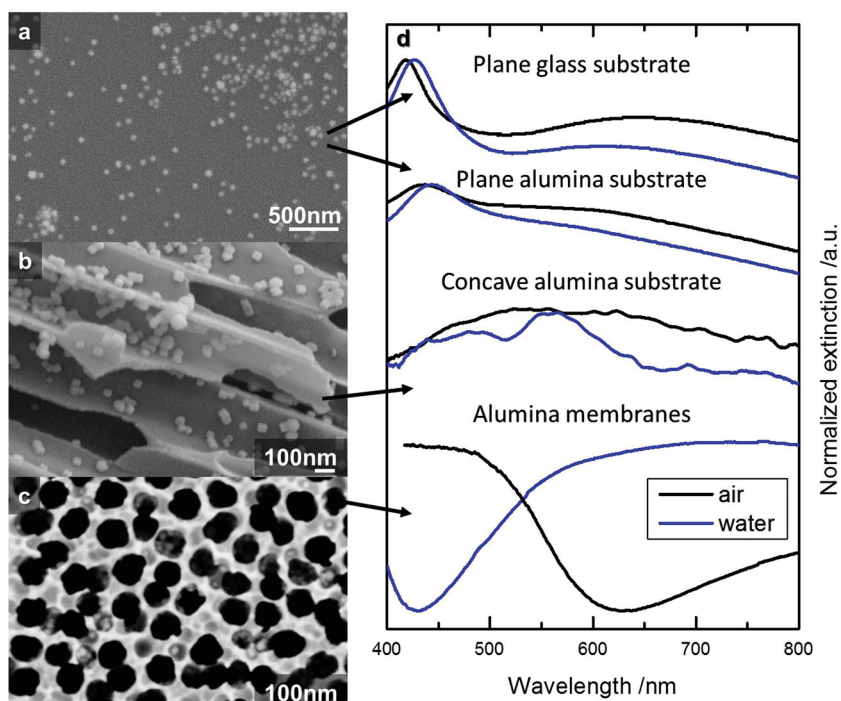


Figure 1. SEM images of silver nanocubes deposited on a) a planar glass/alumina substrate, b) a concave alumina substrate obtained by fracturing a porous alumina membrane, and c) a porous alumina membrane. d) Normalized optical extinction spectra of the corresponding nanocube-substrate assemblies in air or water immersion media.

nanocubes deposited onto various substrates. Besides planar substrates of glass and alumina, we considered concave alumina substrates and porous alumina membranes. **Figure 1** shows typical SEM images of the morphologies of nanocube deposits along with corresponding optical extinction spectra. It can be seen that for the planar and concave substrates (Figure 1a,b, respectively), nanocubes essentially form a monolayer, with both single and aggregated particles in evidence. For the porous alumina substrate (Figure 1c), nanocubes were bound to the interior walls of the cylindrical pores of the 60- μm thick membrane, again with various degrees of aggregation. The influence of these nanocube-substrate morphologies on the optical extinction spectra and refractive index sensitivity is seen to be quite dramatic (Figure 1d). For the case of planar substrates, the optical extinction spectra are characterized by a fairly narrow peak at 400–450 nm and a broad feature at wavelengths longer than 500 nm. The latter feature transitions from being a peak when glass is the substrate to a shoulder when alumina is the substrate.

For the case of nanocubes deposited on concave alumina substrates (formed by the longitudinal fracture of porous alumina membranes), a broad resonance centered at 550–600 nm is observed with rather little dependency on the immersion medium. Finally, the optical extinction spectra of nanocube infiltrated porous alumina membranes can be seen to strongly depend on the surrounding medium. For measurements in air, high extinction at short wavelengths decreasing to a minimum at around 630 nm is seen. On the other hand, when water is the medium, a broad peak in the range 600–800 nm appeared, which does not exist under dry conditions.

This large change in the extinction spectrum on switching air with water can be expressed as a refractive index sensitivity of 770 nm RIU^{-1} , more than an order of magnitude larger than that observed for the case of planar substrates (30 nm RIU^{-1}). To account for this quite unprecedented improvement in the sensing capabilities of silver nanocubes, we carried out a systematic theoretical study based on FDTD simulations. In order to provide as realistic information as possible, we recognized from microscopic studies that our model should include a) substrate type (and therefore refractive index) (section 3.1), b) nanocube aggregation state (3.2), c) substrate curvature (3.3), and d) nanocube plasmonic coupling through pore walls (3.4). In the following sections, we will systematically introduce these features in order to build up a picture of their contribution to the optical properties in general and the refractive index sensitivity in particular.

An important factor for the plasmonic properties of nanocubes is the sharpness of the edges and corners. Processing and synthesis of the nanocubes typically results in a small degree of rounding of the edges, which can dramatically affect the optical absorption. To model the experimental extinction results, an edge rounding factor of 15% and a PVP coating of 2 nm were chosen based upon TEM analysis of the nanocubes (Figure S2, Supporting Information). It should be noted that a higher sensitivity could be reached by using perfect cubes with no edge rounding and a small cube-to-cube distance.^[36] A AgNC with less edge rounding results in a higher extinction cross-section, smaller peak width, and more primitive cube modes,^[37,38] due to better surface charge separation and in the presence of a substrate, a distinct hybridization of the cube modes.^[21]

3.1. Effect of Substrate on Chemical Sensing

As we observed in computer simulations, the primitive dipole and quadrupolar nanocube modes are not well-separated due to edge rounding and the cube-substrate spacing resulting from the presence of the 2 nm PVP coating of nanocubes (Figure 2). This discussion is focused on the cube modes, which have a plasmonic peak between 400 and 500 nm. With an increase in the substrate refractive index (n_s), the primitive dipole mode is hybridized into bonding, anti-bonding, and higher order cube modes. This hybridization of the cube modes can be attributed to interference between the dark and bright plasmon modes.^[22] In the extinction spectra of an AgNC surrounded by air, only the primitive cube modes appear, as shown by the surface charge distribution plots in Figure 2b (i: primitive dipole mode, ii–iii: higher dipole modes). The surface charge distributions

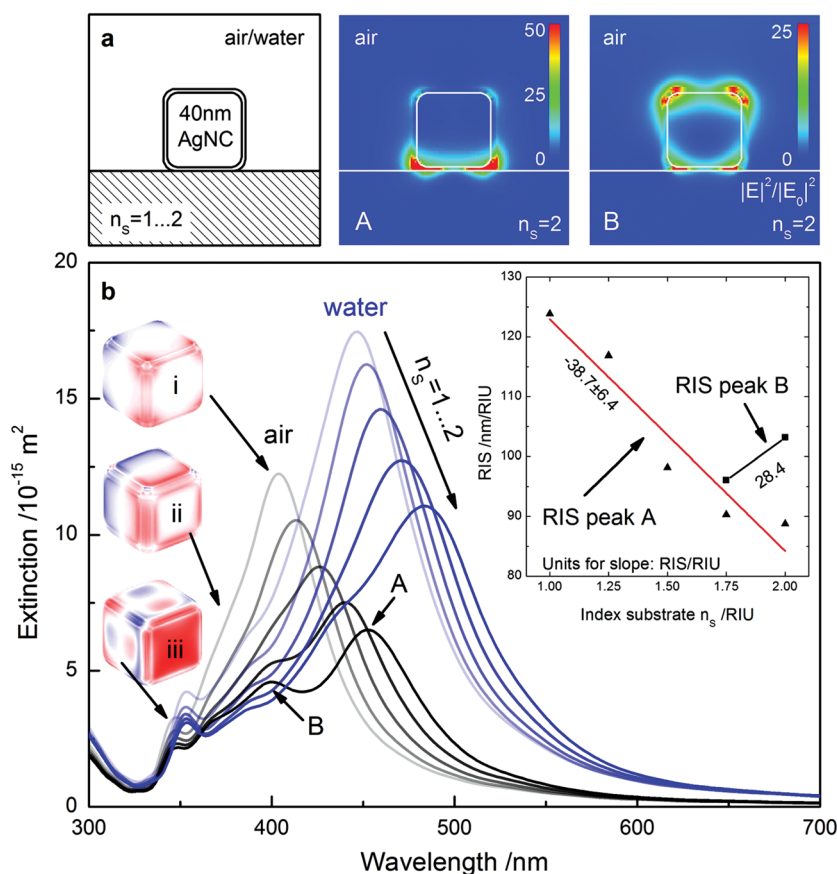


Figure 2. a) Theoretical model of a PVP-coated silver nanocube on a planar substrate used for determination of the optical properties. For the case of a substrate refractive index of 2 and medium refractive index of 1 (air), subframe A and B show the bonding and anti-bonding modes of the nanocube at 450 nm and 400 nm, respectively. b) Simulated extinction spectra for the model shown in (a) with substrate refractive index at 0.25 unit increments. The schematics i, ii, and iii show the charge distribution of the primitive resonant features. The inset shows the dependency of the refractive index sensitivity on substrate refractive index for modes A and B. Note that for the latter case, resolution of resonance is only possible for substrate indices of 1.75 and 2.

(i–iii) shown in Figure 2b were extracted at the PVP–air interface and the color scale was arbitrarily chosen for clarity. A systematic increase of the substrate refractive index results in a steady decrease in sensitivity (see inset in Figure 2b). However, the hybridization of the primitive cube mode allows a relatively better RIS. Essentially, the primitive dipole mode is clearly split into bonding (A) and anti-bonding (B) at a refractive index greater than $n_s = 1.75$.

The anti-bonding mode is more sensitive to the environment in comparison with the bonding mode, due to its orientation towards the medium. For instance, at $n_s = 2$ the peak of the anti-bonding mode shifts 35 nm, which results in a sensitivity of 103 nm RIU^{-1} . The RIS of the anti-bonding mode shows a 16% higher sensitivity compared with the bonding mode. The FoM is a further indicator to determine the quality of a plasmonic sensor. This quality factor is commonly defined as the resonance shift caused by change in the refractive index and normalized to the resonance line width. The simulations show that the FoM of the anti-bonding mode is twice as high as that of the bonding mode (Table S1, Supporting Information).

These preliminary tests are comparable with literature values from Sherry et al., who determined a FoM to be 2.3 times higher for the anti-bonding mode when compared to the bonding mode.^[21]

3.2. AgNC Aggregates on a Planar Glass Substrate

In order to evaluate the experimentally observed plasmonic behavior of nanocube aggregates on a planar glass substrate, we modeled different aggregated clusters based on statistical analysis of nanocube aggregation (Figure S3 and S4, Supporting Information). Table S2 (Supporting Information) summarizes the nanocube aggregates that are considered to be representative of the actual planar substrate. To reproduce the experimental findings, a weight function of the simulated spectra of individual aggregates was used to create a composite spectral signature (2a). For instance, the experimentally measured extinction in air shows a dominant peak at 420 nm, which matches exactly with the simulated single cube spectrum weighted by a factor of 12. The second peak in the experimentally measured spectra is due to nanocube clusters with a greater number of particles and consequently, is referred to as the “aggregation-peak.”^[39] The aggregation-peak is dominated by the longitudinal modes of coupled trimer, tetramer, and pentamer aggregates (Figure 3b). Plasmonic contributions from nanocube aggregates in dense regions are not considered here because corresponding LSPR phenomena are probably located outside of our experimental range of spectral measurements (above 1000 nm).

The transverse and longitudinal modes are defined according to the geometrical axes of the nanocube assemblies. Only a few basic aggregate configurations could be simulated; however, these aggregates can be used to obtain a good match with the experimental findings. The initial weight function values were determined using the statistical analysis of the aggregate types determined from SEM images. The weight function parameters were adjusted iteratively to obtain the qualitatively best fit. Generally, the RIS value was experimentally determined by the dipole mode shift in three different media: air, water, and ethanol. The dipole mode shift is assumed to be linear with refractive index change as demonstrated in literature.^[30] Therefore, considering computational resources available, the extinction spectra were simulated in air and water only (Figure 3b). The measured blue-shift in Figure 3a of the aggregation peak in water behaves contrary to the assumption. This measurement

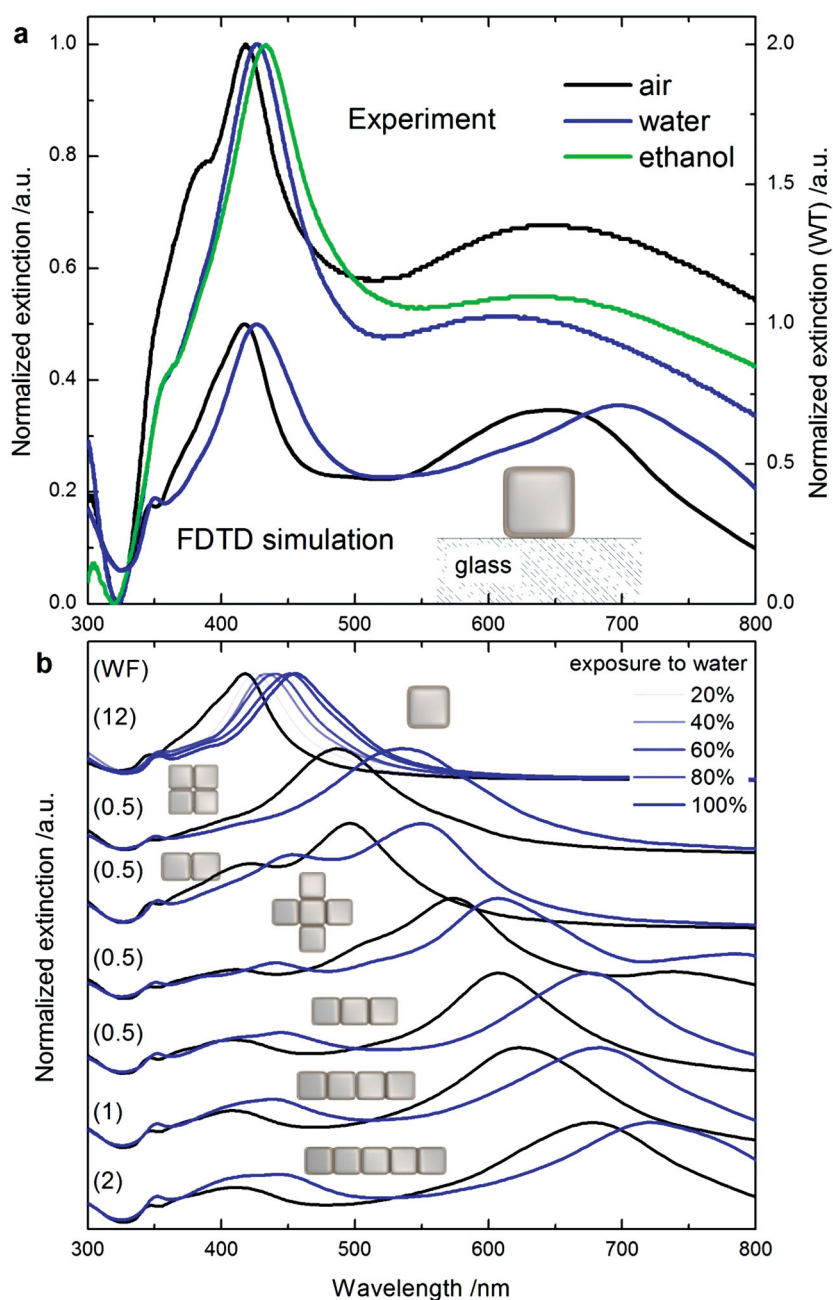


Figure 3. a) Experimentally observed and theoretically calculated extinction spectra of AgNCs on a planar glass substrate for different media. b) Types of aggregates and their extinction spectra used to fit the experimentally observed extinction spectra. Weight function values indicated in parentheses in b.

error could be corrected by exposure the same sample with ethanol, which shows the expected red-shift due to an increased refractive index. The RIS value depends largely on the type of aggregate and shows the highest sensitivity for trimer aggregates and the lowest for cross assemblies (190 and 100 nm RIU⁻¹, respectively). All theoretical sensitivities determined by the FDTD simulation are summarized in Table S2 (Supporting Information). The RIS average of the non-weighted simulated assemblies was found to be 145 ± 30 nm RIU⁻¹ and is higher

than the weighted average, $127 \pm 26 \text{ nm RIU}^{-1}$. The weighted average sensitivity is reduced due to the large contribution of single nanocubes, which have an RIS of 118 nm RIU^{-1} .

Experimentally, the measured sensitivity was discovered to be four times lower than predicted by the FDTD simulation for an individual nanocube in water (Figure 3a). In the simulation shown in Figure 3b, different wetting scenarios were simulated and show that the LSPR mode is blue-shifting by a decrease in cube wetting. The wettability of the nanocube is described here as a percentage and defined as follows: 20% wetting is equal to water covering the top of the cube only, and each further 20% indicates one additional cube face is covered by water. The experimental agreement with 20% wetting indicates that the AgNCs are covered with a possibly heterogeneous water layer. The extinction spectra of the substrates obtained before and after exposure to water suggest that no leaching of AgNCs from the substrates occurred. Additionally, we measured the extinction spectra in ethanol, which shows the expected red-shift as a result of an increased refractive index of the surrounding medium (Figure 3a).

A comparison of the observed RIS values with literature values shows there is potential to increase the sensitivity by reducing the edge rounding, PVP coating, or both. Ianoul and co-workers measured $176 \pm 14 \text{ nm RIU}^{-1}$ for 40 nm AgNCs without a PVP coating on a glass substrate. FDTD simulations show that this value could also be reached by reducing the edge rounding to zero for a 2 nm PVP coating. Currently, the role of PVP coating in sensitivity and stability of nanocubes is unclear.

3.3. AgNC Aggregates on Planar and Concave Alumina Substrate

The plasmonic properties of silver nanocube aggregates deposited on both planar and concave alumina surfaces were used to determine the influence of the substrate refractive index. It is important to note that the sensitivity factor of the dipole mode decreases when the refractive index of the substrate is increased (Figure 2b, inset). This decrease was experimentally observed for a substrate refractive index increase from a flat glass substrate ($n_s = 1.47$, Figure 3a) to a flat alumina substrate ($n_s = 1.78$, Figure S5a, Supporting Information). The weight function values of the modeled aggregates are shown in Figure S5b (Supporting Information). The initial values for the weight function were taken from the statistical analysis shown in Figure S3, S4 (Supporting Information). The experimentally measured RIS value for flat alumina is also 20% of the theoretically expected RIS, which could possibly be attributed to incomplete wetting as discussed above. The sensitivity was theoretically determined to be the highest for a trimer aggregate (162 nm RIU^{-1}) and the lowest for a single cube (92 nm RIU^{-1}). The weighted average RIS value for a flat alumina substrate is $107 \pm 20 \text{ nm RIU}^{-1}$ (determined from simulation results). A more detailed discussion about AgNC aggregates on a concave alumina substrate could be found in the Supporting Information (see discussion and Table S2).

3.4. The Inter-Pore Coupling Effect

We suggest that plasmon coupling of nanocubes aggregated on the walls of neighboring cylindrical pores might be

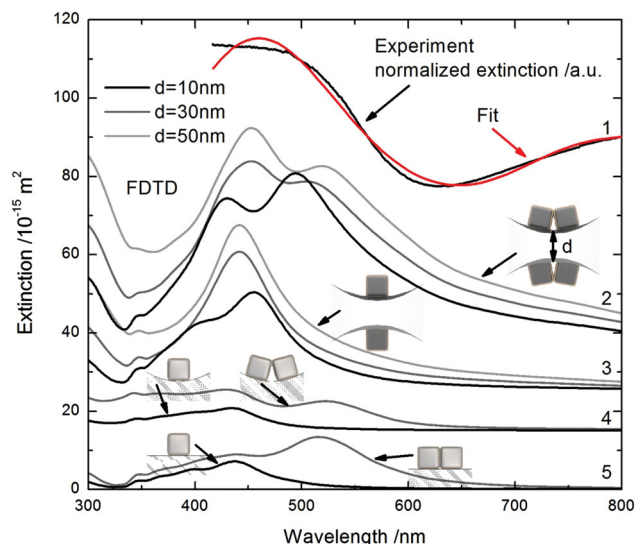


Figure 4. 1) Experimental extinction spectrum of AgNCs in a porous alumina substrate. 2,3) Types of aggregates and their extinction spectra that contribute to the inter-pore coupling effect. 4,5) Other types of aggregates and their corresponding extinction spectra.

a contributing factor to the increased RIS in porous alumina substrates. This inter-pore coupling can arise if two or more nanocubes are located opposite one another across a pore wall and are thus separated by an alumina layer with a thickness of 40 nm (see inset images in Figure 4).

Figure 4 shows the experimental extinction spectrum (1) of AgNCs bound within PAMs in air and the corresponding simulations for different aggregates (2–5). The shape and peak positions of the experimentally observed extinction spectra can be simulated by only considering contributions from plasmonic amplification^[40] based on plasmonic field coupling between the AgNCs located on the alumina pore walls. This plasmonic amplification can clearly be seen in Figure 4 where the extinction cross-section is about 13 ± 3 times higher in the case of inter-pore coupling compared with the LSPR of AgNC assemblies on a flat alumina substrate. Two cases of inter-pore coupling and two cases of AgNC aggregates are compared in this figure. Extinction spectra can be compared for “dimer–dimer” coupling (2), “monomer–monomer” coupling (3), a AgNC assembly on a concave alumina substrate (4), and a AgNC assembly on a flat alumina substrate (5).

It is clear that the simulated inter-pore coupling effects show all characteristic features of experimental extinction spectra (Figure 4). For instance, the case of the “monomer–monomer” configuration at different alumina wall thicknesses was considered (line 3 in Figure 4). In the case of a 10 nm distance between the cubes, we observe two significant extinction peaks, which could be attributed to a transverse mode at 394 nm and a longitudinal mode at 456 nm (see the cross-section distribution shown in Figure 4). Both modes overlap with increasing alumina wall thickness to the experimentally measured peak position (at 436 nm). The longitudinal mode for this arrangement shows high-intensity fields oriented towards the medium (Figure 5). All inter-pore coupling plots

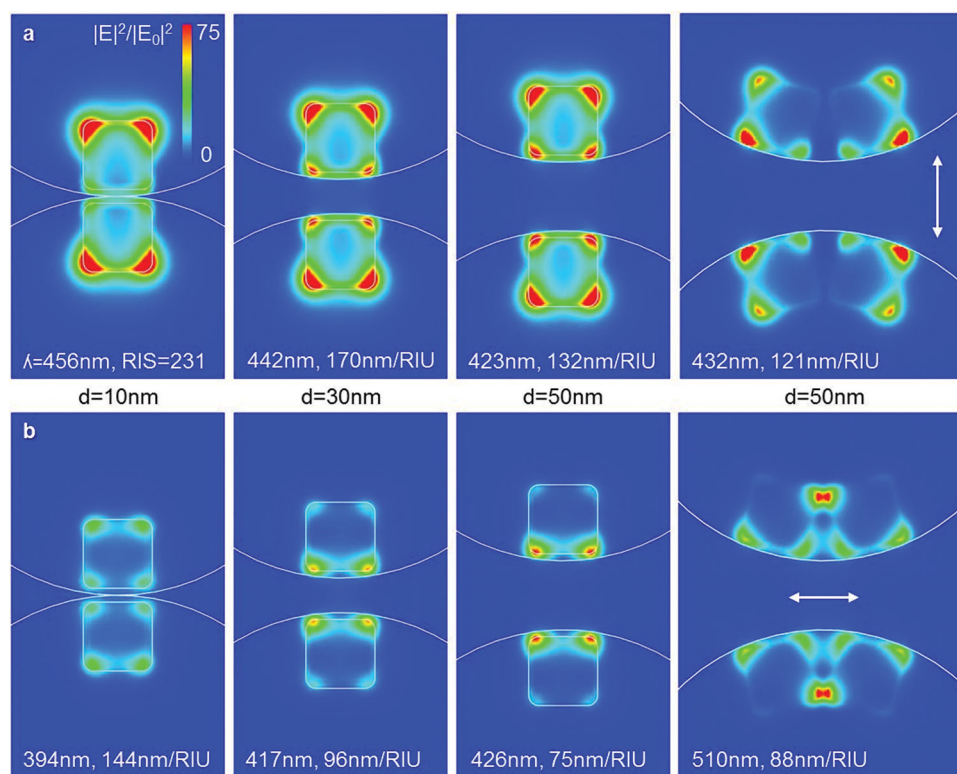


Figure 5. Possible “monomer–monomer” and “dimer–dimer” nanocube coupling effects at different thicknesses of the alumina wall. Polarization orientations a) along and b) perpendicular to the cube orientation axis are shown by arrows.

possess the similar characteristic of a mirror image across a central horizontal axis. This specific field orientation is a necessary condition for the high RIS value of these simulations. The transverse mode can generally be described as an intensity field orientated towards the pore wall (Figure 5). For more complex structures such as a “dimer–dimer” configuration, the modes look similar to dimer coupling without inter-pore coupling.

As expected, “monomer–monomer” nanocube coupling shows the highest RIS value (230 nm RIU⁻¹ at $d = 10$ nm, longitudinal mode) due to the orientation of the intensity fields and the maximum amount of contact faces exposed to the medium. Compared with a single AgNC on a flat alumina or a concave alumina substrate, the RIS is 2.5 and 1.6 times higher, respectively, in the case of inter-pore coupling. The FDTD simulation shows this trend of a higher RIS value due to the inter-pore coupling effect but it still underestimates the experimentally measured value by a factor of 3. This difference can possibly be attributed to a limited representation of all possible AgNC aggregates within various cylindrical pores.

Very different extinction behavior is observed for aggregated nanocubes in water (Figure 6). The broad extinction peak around 700 nm can be described by three Lorentzian functions, which can be related to trimers, tetramers, pentamers, and more complex aggregates. For simulations, these aggregate types were located at the concave alumina wall and were exposed along the cylindrical pore, which is identical to the

experimental setup. The aggregation examples of cross aggregation, tetramer and pentamer arrangements, which are shown in Figure 6, are determined without plasmonic field coupling through the alumina walls. Examples from “monomer–monomer” and “dimer–dimer” structures have shown that the intensity significantly increases when the modes couple through an alumina wall (plasmonic amplification). Consequently, simulation with more complex structures which are coupled through the alumina pore walls should support this complex aggregation peak in water.

The envelope mode function (clusters of closely located plasmonic modes related to different types of aggregates) can be approximated by a Lorentzian function with a peak at 439 nm and FWHM of 325 nm, which results in an RIS of 767 nm RIU⁻¹ and a FoM of 2.4. The theoretically determined FoM is 3.8 for a “monomer–monomer” setup separated by a distance of 10 nm. These FoM values are comparable with quadrupolar cube mode sensing.^[18] We found that the RIS determined by the inter-pore coupling effect is higher than ever previously reported for 40 nm AgNCs. From the deconvolution of the inter-pore coupling peak in water using three Lorentzian functions, we can assign the first Lorentzian as “monomer–monomer” coupling and the Lorentzian peaks (2) and (3) as complex face-to-face aggregates that are amplified through the inter-pore coupling effect.

Compared with flat surfaces and concave substrates the refractive index sensitivity for porous substrates are much more reliable due to the following reasons: First, due to

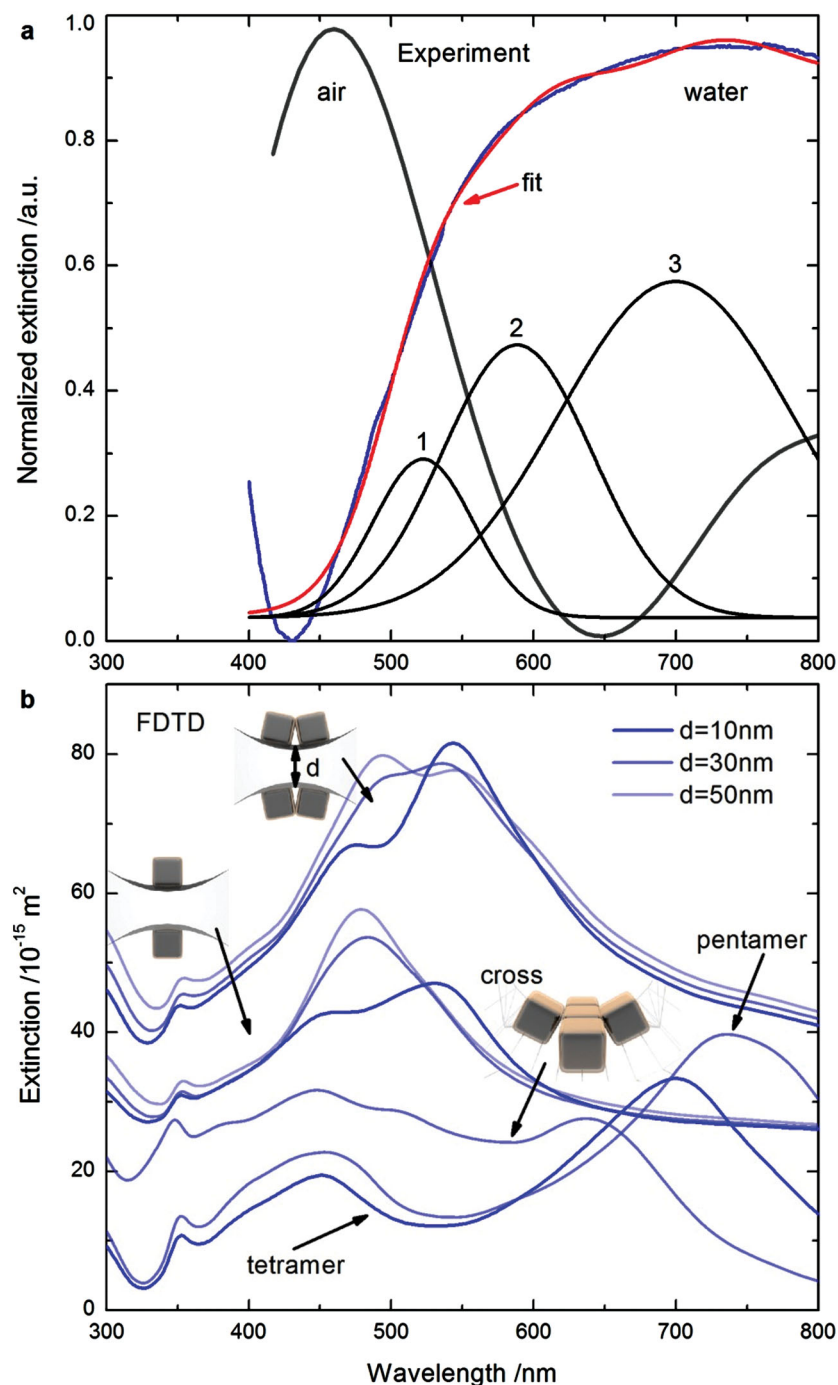


Figure 6. a) Experimental extinction spectrum of a AgNC-decorated porous alumina substrate in water (blue) including a three peak (1–3) Lorentzian fit (red) for the water spectrum as well as the fit for the air spectrum (gray). b) Types of aggregates and their extinction spectra that contribute to the inter-pore coupling effect within a porous alumina substrate as well as other types of nanocube aggregates (cross, tetramer, and pentamer) that occur within concave alumina substrates.

the inter-pore coupling effect, we observe a stronger signal response compared to the concave setup. Second, the wettability behavior for porous alumina membranes is different from the other setups. Reasons for the very good wettability

sensitivities by replacing the nanocube aggregates with hollow nanostructures such as nanoframes or with high-aspect-ratio structures such as nanostars or nanorice as can be explored in forthcoming studies.

of the pore setup are due to the capillary attraction of water into the pores, extreme hydrophilicity of the aluminum oxide as well as the ultrathin polymer coating of the inner pore walls with a hydrophilic polyelectrolyte (polyethylenimine (PEI)). Third, the membrane setup records aggregation events over an extended pore depth of 60 μm and the pore itself can act as waveguide. Surprisingly, the numerical simulation underestimates the experimental measured record sensitivity. Reason therefore could be found that the plasmonic amplification is more complex as estimated. Especially, the “monomer–monomer” nanocube coupling shows the highest sensitivity. We think more complex monomer arrangement in more as two pores and arrangement along the pore wall should result in proof of the measured sensitivity.

Finally, it is important to highlight that the experimentally measured sensitivity of silver nanocube aggregates in cylindrical pores measured in this study is much higher than that usually observed for silver nanocubes or other nanostructures deposited on traditional planar substrates (Figure 7). Moreover, the high sensitivity of aggregated silver nanocubes demonstrated here is comparable or exceeds those reported for known structures with the highest sensitivity such as gold nanorod arrays^[41] or gold nanorice nanoparticles.^[9]

4. Conclusions

We reported an extremely high plasmonic sensitivity of about 770 nm per refractive index unit for silver nanocube aggregates distributed within cylindrical pores in contrast to traditional flat substrates. Different aggregation scenarios ranging from individual silver nanocubes to multiple nanocube aggregates on a flat glass surface, a flat and concave alumina substrate as well as a porous alumina substrate were fabricated, experimentally studied and simulated with FDTD to understand the origin of this phenomenon. These results show that with a simple setup of nanoparticle aggregates with fixed separation, a dramatic increase in sensitivity can be obtained. This kind of nanostructure design could show even greater sensing potential with record chemical sen-

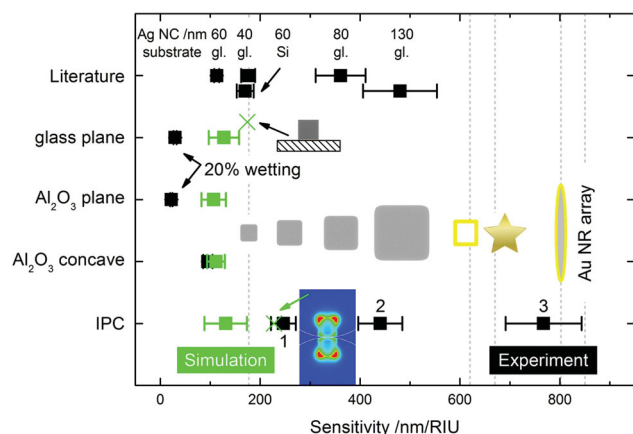


Figure 7. RIU sensitivities measured and calculated for 40 nm silver nanocubes including the sensitivities of gold nanorod arrays and gold nanorice. Literature values are from: AgNC 40–130 nm on glass from lanoul et al.^[42] AgNC 60 nm on glass from El-Sayed et al. includes PVP coating^[43] and AgNC 60 nm on silicon from lanoul and co-workers.^[42] The gold nanostars value is from Hafner et al.^[44] and the gold nanoframe value is from El-Sayed et al.^[45]

Supporting Information

Supporting Information is available from the Wiley Online Library or from the author.

Acknowledgements

Financial support from the US Department of Energy, Office of Basic Energy Sciences, Division of Materials Sciences, and Engineering under Award # DE-FG02-09ER46604 is gratefully acknowledged. We thank Dr. C. Fuentes-Hernandez and J. Hsu from the Bernard Kippelen group (GT) for providing us with alumina-coated substrates. Z.A.C. thanks support under and awarded by Air Force Office of Scientific Research, National Defense Science and Engineering Graduate (NDSEG) Fellowship, 32 CFR 168a. We thank the Partnership for an Advanced Computing Environment (PACE) for computer resources.

Received: June 11, 2013

Revised: July 14, 2013

Published online: September 11, 2013

- [1] a) K. A. Willets, R. P. van Duyne, *Ann. Rev. Phys. Chem.* **2007**, *58*, 267; b) S. A. Maier, P. G. Kik, H. A. Atwater, S. Meltzer, E. Harel, B. E. Koel, A. A. G. Requicha, *Nat. Mater.* **2003**, *2*, 229; c) J. N. Anker, W. P. Hall, O. Lyandres, N. C. Shah, J. Zhao, R. P. Van Duyne, *Nat. Mater.* **2008**, *7*, 442; d) A. M. Funston, C. Novo, T. J. Davis, P. Mulvaney, *Nano Lett.* **2009**, *9*, 1651; e) R. Elghanian, J. J. Storhoff, R. C. Mucic, R. L. Letsinger, C. A. Mirkin, *Science* **1997**, *277*, 1078; f) J. A. Schuller, E. S. Barnard, W. Cai, Y. C. Jun, J. S. White, M. L. Brongersma, *Nat. Mater.* **2010**, *9*, 193; g) R. A. Alvarez-Puebla, L. M. Liz-Marzan, *Small* **2010**, *6*, 604.
- [2] a) Y. N. Xia, P. D. Yang, Y. G. Sun, Y. Y. Wu, B. Mayers, B. Gates, Y. D. Yin, F. Kim, Y. Yan, *Adv. Mater.* **2003**, *15*, 353; b) S. M. Morton, D. W. Silverstein, L. Jensen, *Chem. Rev.* **2011**, *111*, 3962; c) N. J. Halas, S. Lal, W.-S. Chang, S. Link, P. Nordlander, *Chem.*

- Rev.* **2011**, *111*, 3913; d) I. Tokarev, S. Minko, *Soft Matter* **2012**, *8*, 5980; e) I. Luzinov, S. Minko, V. V. Tsukruk, *Soft Matter* **2008**, *4*, 714.
- [3] a) R. Kodiyath, J. Wang, Z. A. Combs, S. Chang, M. K. Gupta, K. D. Anderson, R. J. C. Brown, V. V. Tsukruk, *Small* **2011**, *7*, 3452; b) H. Ko, S. Singamaneni, V. V. Tsukruk, *Small* **2008**, *4*, 1576; c) H. Ko, V. V. Tsukruk, *Small* **2008**, *4*, 1980; d) S. Chang, H. Ko, R. Gunawidjaja, V. V. Tsukruk, *J. Phys. Chem. C* **2011**, *115*, 4387; e) H. Ko, S. Chang, V. V. Tsukruk, *ACS Nano* **2009**, *3*, 181; f) S. Chang, Z. A. Combs, M. K. Gupta, V. V. Tsukruk, *ACS Appl. Mater. Int.* **2010**, *2*, 3333; g) R. Kodiyath, T. A. Papadopoulos, J. Wang, Z. A. Combs, H. Li, R. J. C. Brown, J.-L. Brédas, V. V. Tsukruk, *J. Phys. Chem. C* **2012**, *116*, 13917.
- [4] M. Lisunova, M. Mahmoud, N. Holland, M. A. El-Sayed, V. V. Tsukruk, *J. Mater. Chem.* **2012**, *22*, 16745.
- [5] a) T. König, L. M. Goldenberg, O. Kulikovska, K. Lazar, J. Stumpe, S. Santer, *Soft Matter* **2011**, *7*, 4174; b) T. König, S. Santer, *Nanotechnology* **2012**, *23*, 155301; c) T. König, S. Santer, *Nanotechnology* **2012**, *23*, 485304; d) T. König, Y. N. Sekhar, S. Santer, *Plasmonics* **2012**, *7*, 535; e) T. König, Y. N. Sekhar, S. Santer, *J. Mater. Chem.* **2012**, *22*, 5945; f) T. König, V. V. Tsukruk, S. Santer, *ACS Appl. Mater. Interfaces* **2013**, *5*, 6009.
- [6] a) K. R. Catchpole, *Opt. Express* **2008**, *16*, 21793; b) V. E. Ferry, L. A. Sweatlock, D. Pacifici, H. A. Atwater, *Nano Lett.* **2008**, *8*, 4391.
- [7] C. L. Haynes, R. P. Van Duyne, *J. Phys. Chem. B* **2001**, *105*, 5599.
- [8] K.-S. Lee, M. A. El-Sayed, *J. Phys. Chem. B* **2005**, *109*, 20331.
- [9] H. Wang, D. W. Brandl, F. Le, P. Nordlander, N. J. Halas, *Nano Lett.* **2006**, *6*, 827.
- [10] M. Rycenga, C. M. Cobley, J. Zeng, W. Li, C. H. Moran, Q. Zhang, D. Qin, Y. Xia, *Chem. Rev.* **2011**, *111*, 3669.
- [11] J. M. Romo-Herrera, R. A. Alvarez-Puebla, L. M. Liz-Marzan, *Nanoscale* **2011**, *3*, 1304.
- [12] X. Qian, X. Zhou, S. J. Nie, *J. Am. Chem. Soc.* **2008**, *130*, 14934.
- [13] a) B. Kim, S. L. Tripp, A. Wei, *J. Am. Chem. Soc.* **2001**, *123*, 7955; b) R. Gunawidjaja, S. Peleshanko, H. Ko, V. V. Tsukruk, *Adv. Mater.* **2008**, *20*, 1544; c) H. Ko, V. V. Tsukruk, *Small* **2008**, *4*, 1980.
- [14] J. M. Romo-Herrera, R. A. Alvarez-Puebla, L. M. Liz-Marzan, *Nanoscale* **2011**, *3*, 1304.
- [15] M. A. Mahmoud, C. E. Tabor, M. A. El-Sayed, *J. Phys. Chem. C* **2009**, *113*, 5493.
- [16] a) S. M. Nie, S. R. Emery, *Science* **1997**, *275*, 1102; b) K. Kneipp, Y. Wang, H. Kneipp, L. T. Perelman, I. Itskan, R. Dasari, M. S. Feld, *Phys. Rev. Lett.* **1997**, *78*, 1667; c) J. P. Camden, J. A. Dieringer, Y. M. Wang, D. J. Masiello, L. D. Marks, G. C. Schatz, R. P. Van Duyne, *J. Am. Chem. Soc.* **2008**, *130*, 12616.
- [17] F. J. Garcia-Vidal, L. Martin-Moreno, T. W. Ebbesen, *Rev. Mod. Phys.* **2010**, *82*, 729.
- [18] L. J. Sherry, S. H. Chang, G. C. Schatz, R. P. Van Duyne, B. J. Wiley, Y. Xia, *Nano Lett.* **2005**, *5*, 2034.
- [19] S. P. Zhang, K. Bao, N. J. Halas, H. X. Xu, P. Nordlander, *Nano Lett.* **2011**, *11*, 1657.
- [20] D. P. Lyvers, J.-M. Moon, A. V. Kildishev, V. M. Shalae, A. Wei, *ACS Nano* **2008**, *2*, 2569.
- [21] C. L. Nehl, H. W. Liao, J. H. Hafner, *Nano Lett.* **2006**, *6*, 683.
- [22] G. Raschke, S. Brogl, A. S. Susha, A. L. Rogach, T. A. Klar, J. Feldmann, B. Fieries, N. Petkov, T. Bein, A. Nichtl, K. Kurzinger, *Nano Lett.* **2004**, *4*, 1853.
- [23] a) N. Grillet, D. Manchon, F. Bertorelle, C. Bonnet, M. Broyer, E. Cottancin, J. Lerme, M. Hillenkamp, M. Pellarin, *ACS Nano* **2011**, *5*, 9450; b) M. Rycenga, C. M. Cobley, J. Zeng, W. Li, C. H. Moran, Q. Zhang, D. Qin, Y. Xia, *Chem. Rev.* **2011**, *111*, 3669.
- [24] C. Tabor, R. Murali, M. Mahmoud, M. A. El-Sayed, *J. Phys. Chem. A* **2009**, *113*, 1946.
- [25] M. A. Mahmoud, M. A. El-Sayed, *J. Phys. Chem. C* **2008**, *112*, 14618.
- [26] M. Lahav, T. Sehayek, A. Vaskevich, I. Rubinstein, *Angew. Chem.* **2003**, *42*, 5575.

- [27] M. L. Bruening, D. M. Dotzauer, P. Jain, G. L. Baker, *Langmuir* **2008**, *24*, 7663.
- [28] C. Jiang, V. V. Tsukruk, *Adv. Mater.* **2006**, *18*, 829.
- [29] V. V. Tsukruk, *Prog. Polym. Sci.* **1997**, *22*, 247.
- [30] K. M. Mayer, J. H. Hafner, *Chem. Rev.* **2011**, *111*, 3828.
- [31] R. Kodiyath, S. T. Malak, Z. A. Combs, T. König, M. A. Mahmoud, M. A. El-Sayed, V. V. Tsukruk, *J. Mater. Chem. A* **2013**, *8*, 2677.
- [32] H. J. Hagemann, W. Gudat, C. Kunz, *J. Opt. Soc. Am.* **1975**, *65*, 742.
- [33] P. B. Johnson, R. W. Christy, *Phys. Rev. B* **1972**, *6*, 4370.
- [34] V. P. Drachev, U. K. Chettiar, A. V. Kildishev, H.-K. Yuan, W. Cai, V. M. Shalaev, *Opt. Express* **2008**, *16*, 2, 1186.
- [35] E. D. Palik, *Handbook of Optical Constants in Solids*, Academic Press, New York **1991**, p.2.
- [36] M. Murali, M. A. Mahmoud, M. A. El-Sayed, *J. Phys. Chem. A* **2009**, *113*, 1946.
- [37] B. J. Wiley, S. H. Im, Z.-Y. Li, J. McLellan, A. Siekkinen, Y. Xia, *J. Phys. Chem. B* **2006**, *110*, 15666.
- [38] J. Zeng, S. Roberts, Y. Xia, *Chem. Eur. J.* **2010**, *16*, 12559.
- [39] M. A. Mahmoud, C. E. Tabor, M. A. El-Sayed, *J. Phys. Chem. C* **2009**, *113*, 5493.
- [40] A. Chen, R. L. Miller, A. E. De Prince, A. Joshi-Imre, E. Shevchenko, L. E. Ocola, S. K. Gray, U. Welp, V. K. Vlasov, *Small* **2012**, *9*, 1939.
- [41] D. P. Lyvers, J.-M. Moon, A. V. Kildishev, V. M. Shalaev, A. Wei, *ACS Nano* **2008**, *2*, 2569.
- [42] a) N. Ahamad, A. Bottomley, A. Ianoul, *J. Phys. Chem. C* **2012**, *116*, 185; b) A. Bottomley, A. Ianoul, *ChemPhysChem* **2011**, *12*, 2912.
- [43] M. A. Mahmoud, M. A. El-Sayed, *J. Am. Chem. Soc.* **2012**, *134*, 6434.
- [44] C. L. Nehl, H. W. Liao, J. H. Hafner, *Nano Lett.* **2006**, *6*, 683.
- [45] M. A. Mahmoud, M. A. El-Sayed, *J. Am. Chem. Soc.* **2010**, *132*, 12704.